Supporting Information for

Effects of Sulfate during CO_2 Attack on Portland Cement and Their Impacts on Mechanical Properties under Geologic CO_2 Sequestration Conditions

Qingyun Li,[1] Yun Mook Lim,[2] and Young-Shin Jun[1], *

[1]*Department of Energy, Environmental and Chemical Engineering, Washington University, St. Louis, MO 63130, USA*

[2] *Department of Civil and Environmental Engineering, Yonsei University, Seoul 120-749, Republic of Korea*

Address: One Brookings Drive, Campus Box 1180

E-mail: ysjun@seas.wustl.edu

Phone: (314)935-4539

Fax: (314)935-7211

http://encl.engineering.wustl.edu/

Environmental Science & Technology

Summary

15 pages, including 3 Tables and 11 Figures.

S1.Experimental setups

A bench-top reactor (Parr Instrument Company, IL) was connected to a syringe gas pump (Teledyne ISCO, Lincoln, NE). The pressure in the reactor was monitored by a barometer (Parr Instrument Company, IL) on the cap of the reactor. A controller connected to an *in situ* thermocouple automatically turning on or off the heater when the temperature in the reactor was lower or higher than the set value. Such system was used in several previous studies in our lab.[1-8]

The initial pH in the reaction, after injecting CO_2 and obtaining high temperature, can be measured by a pH probe designed for high pressures (1–139 bar) and temperatures (20–120 °C) (Corr Instruments, TX).[1, 3, 4, 7, 8] Because our *in situ* pH probe is glass-based, and could be damaged if contacted with a locally basic aqueous environment, we did not monitor the pH increase as a function of time during reactions. Instead, we used Geochemists' Workbench (GWB, Release 8.0, RockWare, Inc.) to calculate the possible evolution of pH in our systems containing CO_2 (Details are available in Section S4.3).

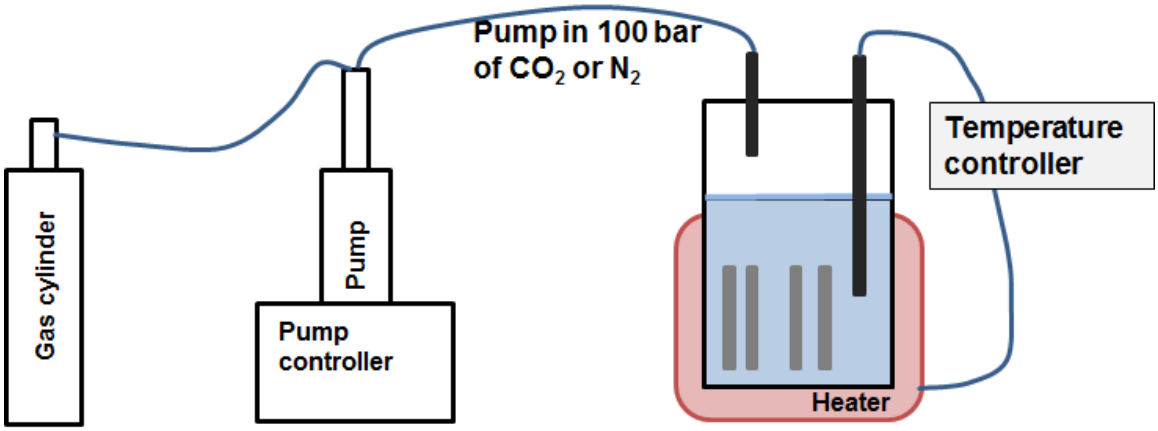

Figure S1 Experimental setup for high temperature/pressure experiments, adopted from our concurrent study.[9] The temperature is controlled at 95°C and the pressure is controlled at 100 bar.

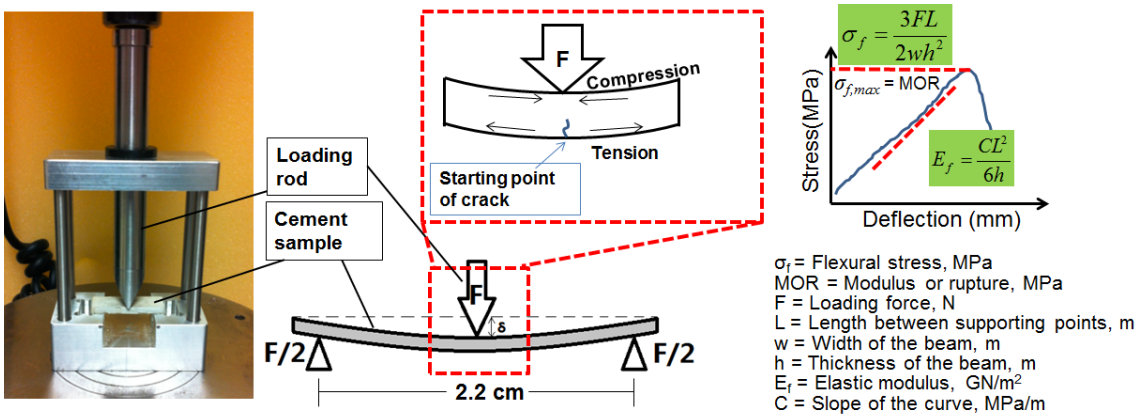

43

44 **Figure S2.** Diagram of three-point bending test, adopted from our concurrent study.[9]
45 Loading force (F) and the deflection of the beam (δ) were recorded. During the bending
46 process, the top surface of the beam has the maximum compression stress, and the bottom
47 surface has the maximum tensile stress. Failure starts from the bottom surface. A typical
48 stress curve is also shown.

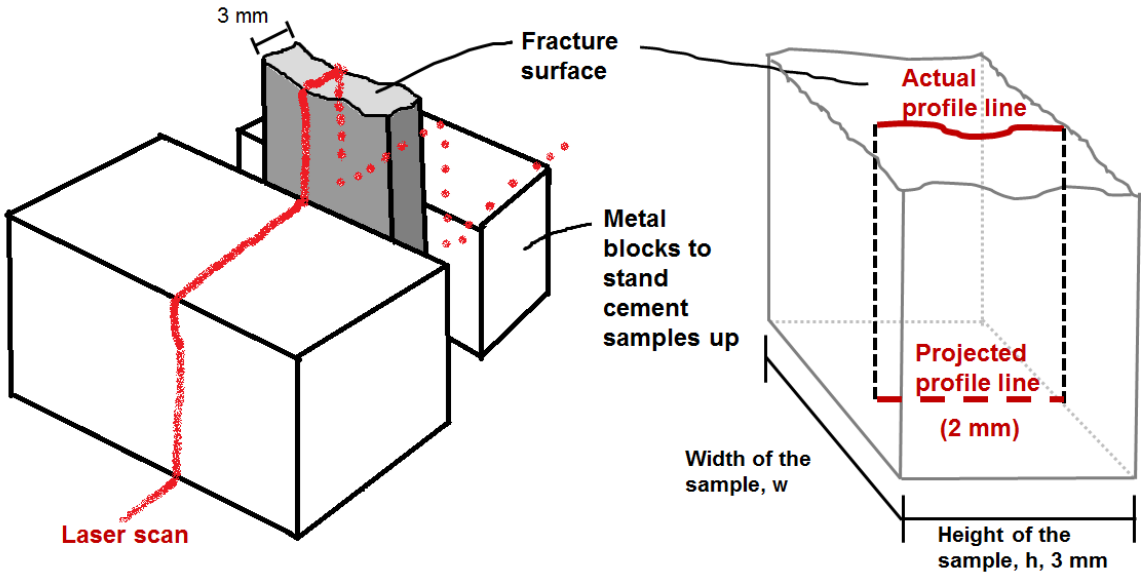

49

50 **Figure S3.** Diagram for quantification of fracture roughness by a laser scanner (left), and
51 an example profile line (right). This figure is adopted from our concurrent study.[9] Each
52 sample has ~ 100 profile lines, with projected lines parallel to the h direction. The profile

line roughness (R_L) is calculated as the ratio of the length of actual profile line to the length of projected line. Each ~ 2 mm profile line is given by 21 points, including the end-points.

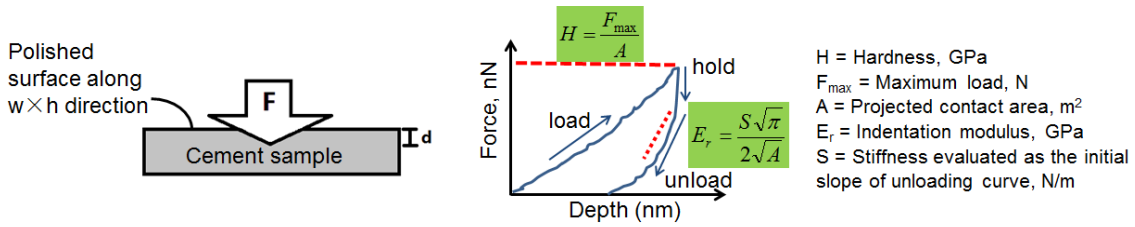

Figure S4. Diagram of nanoindentation, adopted from our concurrent study.[9] A typical indentation curve is shown on the right.

S2 Additional data for chemical analyses

Aqueous concentrations of Ca and Si were measured at the end of the 10 days' reaction (Table S1). The aqueous concentration of Ca should not be used for comparison of cement dissolution under acidic conditions, because they could be much less than the true loss of Ca from the cement samples. During degasing and cooling of the reactor, the high concentrations of Ca formed many secondary precipitates on the surface of the cement samples. These precipitates were removed from the reactor together with the cement sample, without being acidified for ICP measurement. Si is less preferentially leached out, and fewer secondary Si precipitates were observed on the cement samples during sampling. Therefore, Si concentrations likely deviate less than Ca from the real concentrations before degassing and cooling of the system, and they were used to compare relative cement dissolutions.

Table S1 Aqueous concentrations of Ca and Si at the end of the 10 days' reaction. Data for the N2 and the CO2 conditions are from our concurrent study.[9] The positive and negative error bars are the standard deviation of 3 measurements of the same sample by ICP-OES.

Conditions	Ca, mM	Si, mM
N2	9.0 ± 0.3	1.62 ± 0.01
SO4	21.7 ± 0.3	1.64 ± 0.02
CO2	147.6 ± 0.5	5.33 ± 0.03
CO2SO4	234 ± 1	3.70 ± 0.03

Table S2 Thicknesses of different regions of cement attacked by CO_2 in this study.

Condition	Region 2, μm	Region 3, μm	Region 4, μm	Total attacked thickness, μm
CO2	960 ± 100	100 ± 17	170 ± 35	1220 ± 90
CO2SO4	600 ± 17	117 ± 6	80 ± 10	800 ± 6

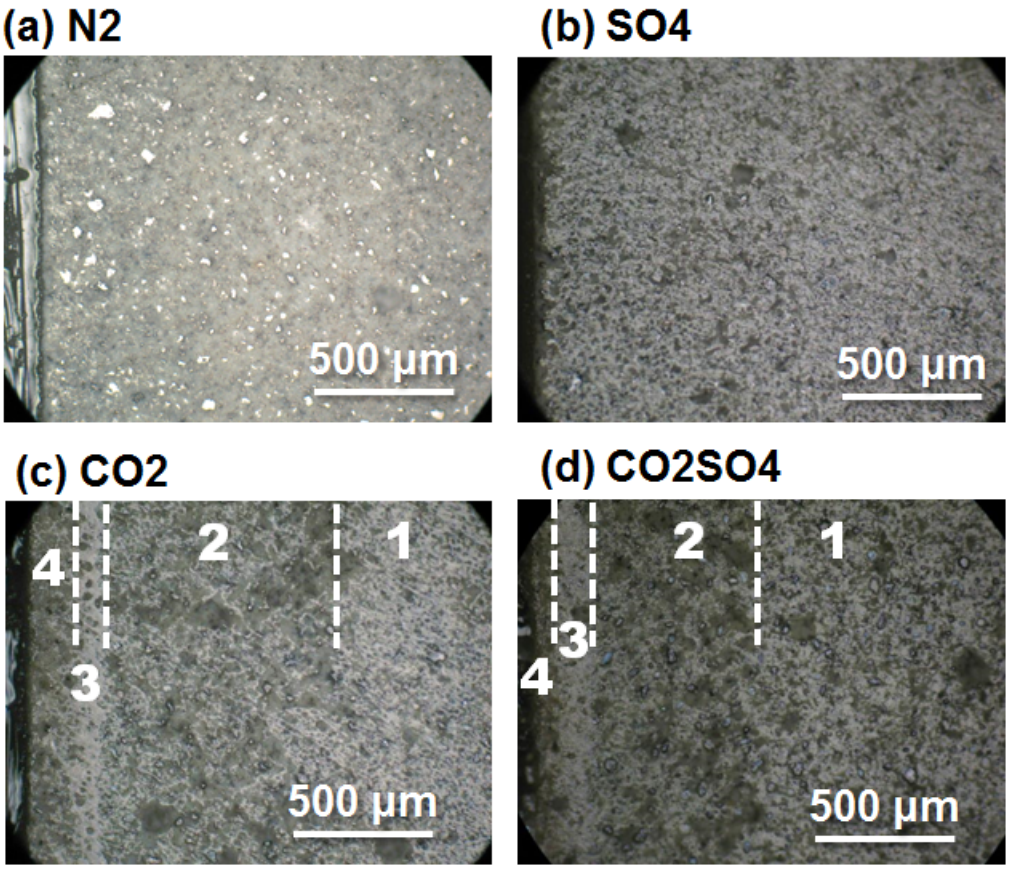

Figure S5. Optical images of polished cross sections of (a) N2, (b) SO4, (c) CO2, and (d) CO2SO4 samples. Images (a) and (c) are adopted from our concurrent study.[9] The SO4 image does not show any evidence of sulfate attack on cement via formation of ettringite and/or gypsum. CO_2 attack on cement under the CO2SO4 condition is less severe than that under the CO2 condition.

S3. Additional data for mechanical property analyses

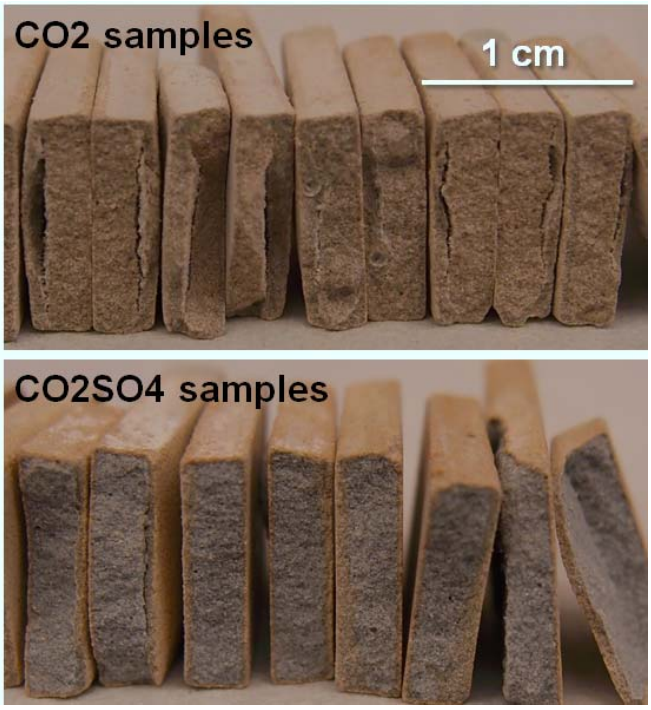

Figure S6. Typical fracture surfaces of the CO2 and CO2SO4 samples. The two pictures were taken with the same background.

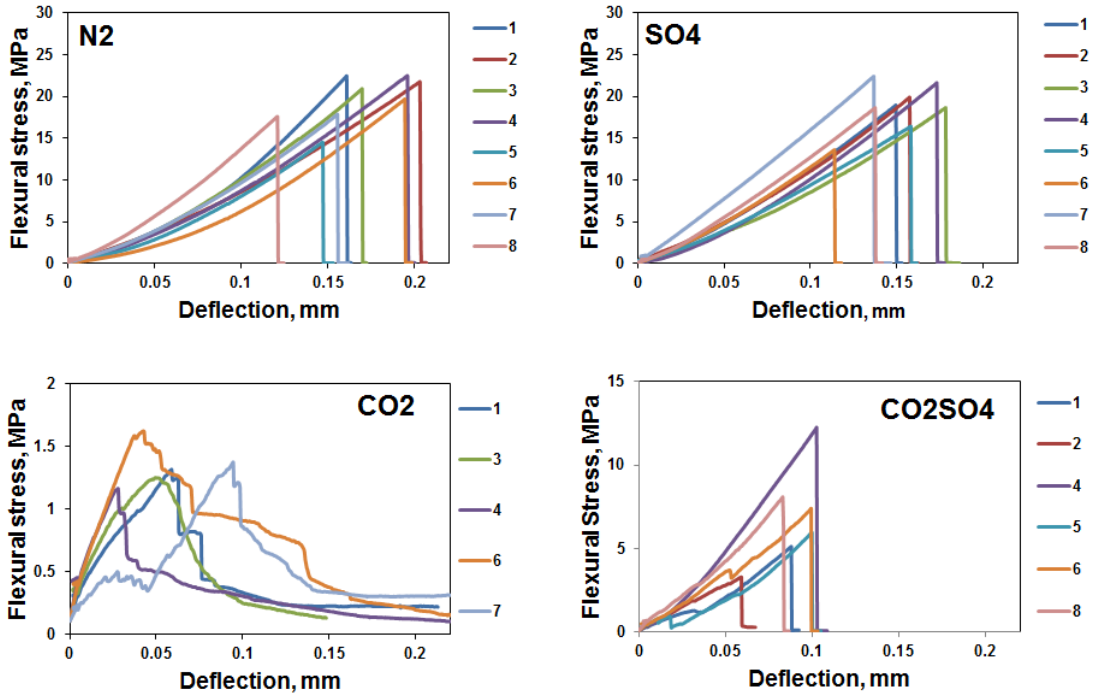

89

90 **Figure S7.** Groups of stress–deflection curves for N2, SO4, CO2, and CO2SO4. Data for
91 N2 and CO2 samples are from our concurrent study.[9] The samples that were already
92 defected before bending tests are not shown.

93

94 **Table S3** Fracture roughness comparison. Data for N2 and CO2 samples are from our
95 concurrent study,[9] and are shown here for comparison. The extent of CO_2 attack on the
96 cement was not sufficient to increase the fracture roughness of the CO2SO4 samples.

Condition	Range of fracture roughness (R_L)	Median R_L	Average R_L
N2	1.00 – 1.05	1.00	1.02
SO4	1.00 – 1.20	1.03	1.06
CO2	1.02 – 2.39	1.14	1.35
CO2SO4	1.00 – 1.35	1.03	1.08

97

98

Hardness and Indentation Modulus

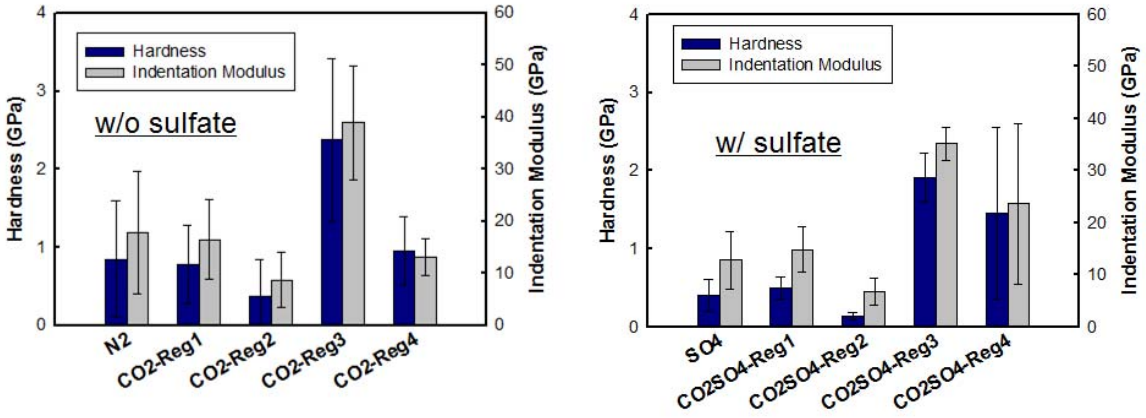

Figure S8 Hardness and indentation modulus. Data for N2 and CO2 samples are from our concurrent study,[9] and are shown here for comparison. Similar to CO2 samples, the carbonated layer (Region 3) in CO2SO4 samples has 2–3 times higher hardness and indentation modulus than the intact core, while Region 2 has decreased hardness and indentation modulus, compared to the intact core. When Region 3 partially dissolves to form Region 4, the hardness and indentation modulus are also decreased.

S4. Additional discussion

S4.1 Post-cracking behaviors of reacted samples

We found that the stress–deflection curves for the CO2 samples dropped gradually after the main crack (Figure S6),[9] while the stress–deflection curves of samples reacted under all other conditions dropped immediately. The gradual drop of the stress–deflection curves of the CO2 samples indicated that the reaction changed the samples from brittle to quasi-brittle, and after the CO_2 attack, although the samples are less strong, they can absorb more energy after the main crack happens and before being completely broken. On the

other hand, the CO2SO4 samples, which also experienced CO_2 attack, had an immediate drop in the stress–deflection curves after crack, indicating the CO_2 attack in these samples was not able to change the post-crack behaviors as it did in the CO2 samples. The difference is consistent with our finding of thinner CO_2 attacked depths from both sides of samples in the CO2SO4 samples (~800 μm) than those in the CO2 samples (~1220 μm). Due to the thinner attacked depth, the CO2SO4 samples had a thicker intact core (~1400 μm) than the CO2 samples (~560 μm). The properties of the intact core are approximated by the control samples. Therefore, the CO2SO4 samples' post-cracking behavior was not the same as that of the CO2 samples, but was closer to the N2 samples.

S4.2 Effects of sulfate on Al-containing phases

The reactions of Al-containing phases in cement (C_3A and C_4AF as solid solution[10]) start with hydration. The hydration of Al-containing phases are related to the time length of early hardening of cement. To slow down this process, a small amount of gypsum needs to be added to the clinker. The retardation effect of gypsum is based on the aqueous sulfate ions released by gypsum. There are two main hypotheses by which gypsum has its retardation effect.[11] One is that a hydrated layer formed together with ettringite, coating on the anhydrous grain which hinders diffusion of water into the grain. The other hypothesis is that the adsorption of sulfate ions onto the active site of Al-containing phases decreases hydration rate of the grain. Except affecting the setting time, the Al-containing phases does not contribute significantly to the mechanical properties of cement. In this study, there are more anhydrous Al-containing phases in SO4 samples than in N2 samples, because the excessive sulfate ions has retarded the hydration of these phases.

A system with Al-containing phases and gypsum may also affect the hydration kinetics of C_2S and C_3S.[11] However, we found that the strength and elastic modulus of N2 and SO4 samples were not significantly different.

Usually the Al-containing phases form ettringite with sulfate species at the early stage of hydration, and later on, as more Al-containing phases are hydrated and help take up sulfate, the ettringite will completely or partially convert to AFm (i.e., alumina, ferric oxide, monosulfate). Later on, with excessive sulfate, AFm will further react with sulfate to form more ettringite. Ettringite is known to have larger volume, and if excessively formed, can cause cracks in cement, which is known as "sulfate attack on cement".[12, 13] In our experimental conditions, the reaction time is 10 days, likely too short for the sulfate attack to reveal, especially when the hydration of Al-containing phases are significantly retarded.

S4.3 Effects of sulfate on the carbonated layer

pH evolution modeled by GWB In this study, due to the fast cement dissolution at acidic pHs in the CO2 and CO2SO4 systems, we expected the pH increase was fast. We used Geochemists' Workbench (GWB, Release 8.0, RockWare, Inc.) to calculate the possible evolution of pH in our systems containing CO_2. Using thermo.dat as the thermodynamic database, the initial brine composition was input as the basis. Values were calculated for 1 L of solution. pH was set to balance the solution charge. The fugacity of CO_2 at 95 ^oC and 100 bar was calculate by Duan's equation to be 75,[14] and was kept constant. To set up the experimentally measured initial pH in GWB, the initial pH of both the CO2 and CO2SO4 conditions were adjusted to be 3.0 by adding a certain amount of Cl^- (i.e., HCl) and letting H^+ balance the charge. Only dissolution of portlandite was

considered. One or ten grams of portlandite were used as the reactant. pH evolution was plotted as a function of amount of portlandite dissolved for both CO2 and CO2SO4 conditions. Both systems had an equilibrium pH of 5.0. Before the equilibrium was reached, the pH of the CO2SO4 samples was lower by 0–0.6 for the same amount of portlandite dissolved. Because we observed slower dissolution of cement under the CO2SO4 condition, the pH difference cannot be the reason for the mitigated CO_2 attack observed in the CO2SO4 system, and there must be other mechanisms to counteract the promotion of cement dissolution by a low pH.

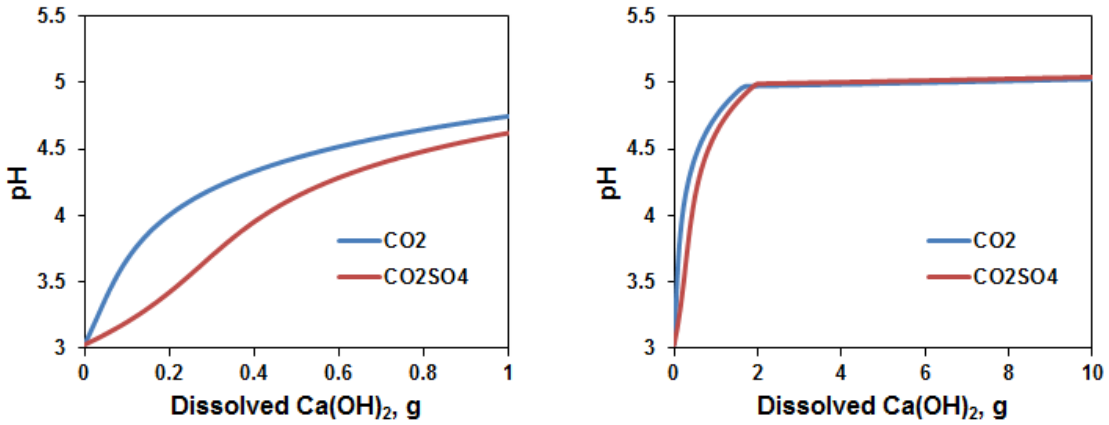

Figure S9. Evolution of pH in CO2 and CO2SO4 systems calculated by GWB.

Observations of calcite reacted with cement samples under the CO2SO4 condition

The distorted rhombohedral precipitates suggest that sulfate affected the precipitation of calcite, which is rhombohedral in a pure $CaCO_3$ system. Because the conductivity of calcite is low (even after AuPd coating), the resolution may not able to resolve the small $CaSO_4$ precipitates on the calcite surface, if there is any. EDS may also collect most of the signal from the bulk calcite by penetrating the potential $CaSO_4$ coating.

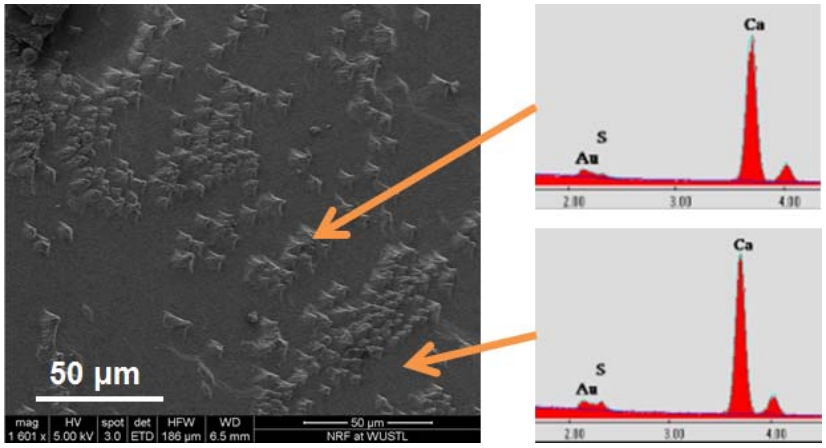

Figure S10. SEM-EDS results for the surface of single crystal calcite grains reacted with cement under the CO2SO4 condition.

BSE-SEM-EDS results for sulfur mapping BSE images were obtained for the Region 3 (carbonated layer) and Region 4 from a CO2SO4 sample. Sulfur mapping by EDS showed that the outer part of Region 3 has slightly more sulfur than the inner part. The region where sulfur is more abundant may have the coating of $CaSO_4$ on $CaCO_3$ grains and adsorption of sulfate on $CaCO_3$ surfaces. However, the sulfur distribution cannot specify which mechanism is the more dominant.

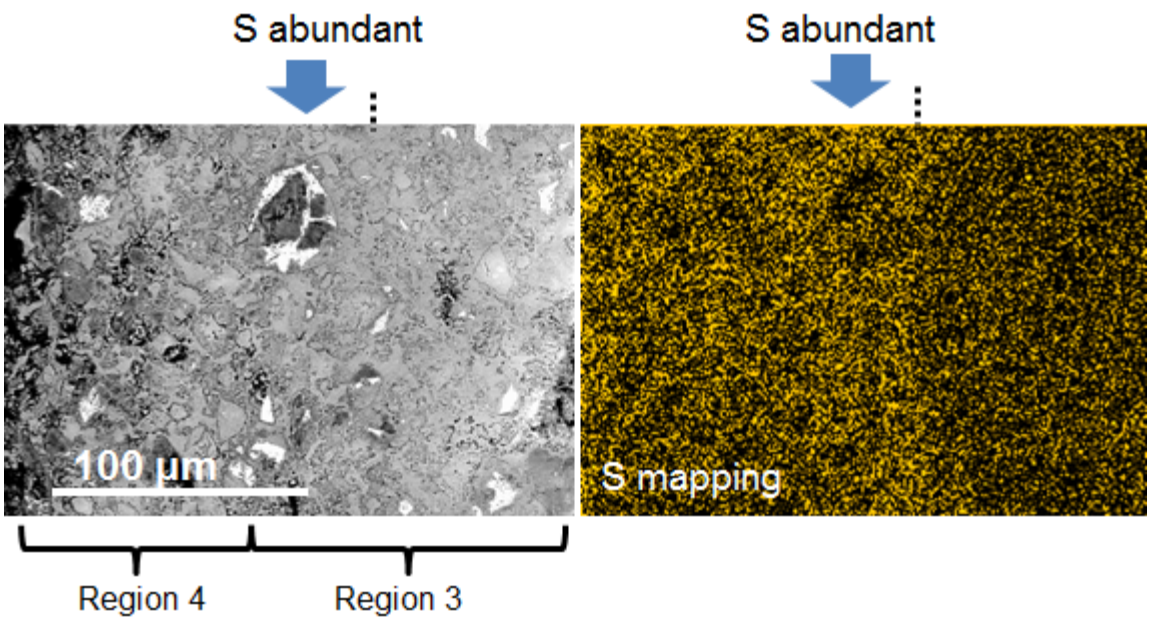

190

191 **Figure S11** BSE images of Region 3 and Region 4 in a CO2SO4 sample, and the sulfur

192 mapping by EDS. The brighter area in the EDS mapping (right) has more S. The outer edge

193 of Region 3 has more S content than inner part of Region 3.

194

References

1. Hu, Y.; Ray, J. R.; Jun, Y.-S., Biotite–brine Interactions under Acidic Hydrothermal Conditions: Fibrous Illite, Goethite, and Kaolinite Formation and Biotite Surface Cracking. *Environ. Sci. Technol.* **2011,** *45*, (14), 6175-6180.
2. Hu, Y.; Ray, J. R.; Jun, Y.-S., Na^{+}, Ca^{2+}, and Mg^{2+} in Brines Affect Supercritical CO_2–Brine–Biotite Interactions: Ion Exchange, Biotite Dissolution, and Illite Precipitation. *Environ. Sci. Technol.* **2012,** *47*, (1), 191-197.
3. Hu, Y.; Jun, Y.-S., Biotite Dissolution in Brine at Varied Temperatures and CO_2 Pressures: Its Activation Energy and Potential CO_2 Intercalation. *Langmuir* **2012,** *28*, (41), 14633-14641.
4. Yang, Y.; Ronzio, C.; Jun, Y.-S., The Effects of Initial Acetate Concentration on CO_2–Brine-Anorthite Interactions under Geologic CO_2 Sequestration Conditions. *Energy & Environmental Science* **2011,** *4*, (11), 4596-4606.
5. Yang, Y.; Min, Y.; Jun, Y.-S., Structure-Dependent Interactions Between Alkali Feldspars and Organic Compounds: Implications for Reactions in Geologic Carbon Sequestration. *Environ. Sci. Technol.* **2012,** *47*, (1), 150-158.
6. Yang, Y.; Min, Y.; Jun, Y.-S., A Mechanistic Understanding of Plagioclase Dissolution Based on Al Occupancy and T–O Bond Length: from Geologic Carbon Sequestration to Ambient Conditions. *Phys. Chem. Chem. Phys.* **2013,** *15*, (42), 18491-18501.
7. Shao, H.; Ray, J. R.; Jun, Y.-S., Effects of Salinity and the Extent of Water on Supercritical CO_2-induced Phlogopite Dissolution and Secondary Mineral Formation. *Environ. Sci. Technol.* **2011,** *45*, (4), 1737-1743.
8. Shao, H.; Ray, J. R.; Jun, Y.-S., Effects of Organic Ligands on Supercritical CO_2-induced Phlogopite Dissolution and Secondary Mineral Formation. *Chem. Geol.* **2011,** *290*, (3), 121-132.
9. Li, Q.; Lim, Y. M.; Flores, K. M.; Jun, Y., Chemical Reactions of Portland Cement with Aqueous CO_2 and Their Impacts on Cement's Mechanical Properties under CO_2 Sequestration Conditions. *Environ. Sci. Technol.* **2015**; DOI: 10.1021/es5063488.
10. Taylor, H. F., *Cement Chemistry*. Thomas Telford: 1997.
11. Quennoz, A., Hydration of C_3A with Calcium Sulfate Alone and in the Presence of Calcium Silicate. **2011**.
12. Skalny, J.; Brown, P., *Sulfate Attack on Concrete*. Taylor & Francis: 2002.
13. Neville, A., The Confused World of Sulfate Attack on Concrete. *Cem. Concr. Res.* **2004,** *34*, (8), 1275-1296.
14. Duan, Z.; Sun, R., An Improved Model Calculating CO_2 Solubility in Pure Water and Aqueous NaCl Solutions from 273 to 533 K and from 0 to 2000 bar. *Chem. Geol.* **2003,** *193*, (3), 257-271.